Available online at www.sciencedirect.com
ScienceDirect
Cryogenics 48 (2008) 112–121
CRYOGENICS
www.elsevier.com/locate/cryogenics

Anisotropic steady-flow hydrodynamic parameters of microporous media applied to pulse tube and Stirling cryocooler regenerators

W.M. Clearman [a], J.S. Cha [a], S.M. Ghiaasiaan [a,*], C.S. Kirkconnell [b]

[a] G.W. Woodruff School of Mechanical Engineering, Georgia Institute of Technology, Atlanta, GA 30332, United States
[b] Raytheon Space and Airborne Systems, El Segundo, CA 90245, United States

Received 12 September 2007; received in revised form 9 January 2008; accepted 9 January 2008

Abstract

The hydrodynamic parameters associated with steady longitudinal and lateral (radial) flow of helium in several widely-used pulse tube and Stirling cryocooler regenerator fillers were measured and correlated in this investigation. Pressure drops in test sections packed with regenerator fillers were experimentally measured. Computational fluid dynamics (CFD) models of the regenerator test sections and their vicinities were developed and simulations were performed in which the regenerator test sections were modeled as porous media. By iterative repetition of the simulations, the longitudinal and radial permeability and Forchheimer inertial coefficients were determined such that they would lead to agreement between experimental measurements and the simulations. The regenerator fillers included 325 and 400 mesh stainless steel screens, stainless steel metal foam, sintered 400 mesh stainless steel screens, and a stack of micromachined perforated plates. The hydrodynamic response of the regenerator fillers were also correlated as friction factors. The results confirm that the aforementioned regenerator fillers are anisotropic.

Keywords: Cryocoolers; Regenerator; Permeability; Inertial coefficient; Steady flow

1. Introduction

The crucial role of the regenerator in pulse tube and Stirling cryocoolers is well recognized and improving the performance of the various types of cryocoolers is of great interest. For pulse tube refrigerators (PTRs) there are several sources of irreversibility [1]. The regenerator in a PTR is a porous metallic structure which is typically the largest source of loss in cryocoolers [2]. Axial heat conduction, thermal saturation, and frictional losses all cause irreversibility. However, it is difficult to accurately predict the impact of these and other solid–fluid interactions within the porous media for periodic flow. To simplify the analysis of these periodic systems, isotropic hydrodynamic parameters associated with steady flow have sometimes been used [3]. It has recently been shown that CFD tools can simulate the entire cryocooler devices under steady and steady-periodic conditions [4–6]. However, the accuracy of these CFD predictions depend strongly on the accuracy of the closure relations they use. The hydrodynamic and heat transfer parameters associated with the interaction between the coolant fluid and the porous regenerator are thus among the most important closure relations, and are relatively poorly understood. This is particularly true about the hydrodynamic and thermal transport parameters associated with periodic flow in microporous structures.

Rigorous analysis of flow in porous media is in principle possible by pore-level simulations. However, such simulations are impractical for design purposes, and microscopic governing equations and boundary conditions are instead transformed into macroscopic governing equations and

* Corresponding author. Tel.: +1 404 894 3746; fax: +1 404 894 8496.
E-mail address: mghiaasiaan@gatech.edu (S.M. Ghiaasiaan).

0011-2275/$ - see front matter © 2008 Elsevier Ltd. All rights reserved.
doi:10.1016/j.cryogenics.2008.01.002

Nomenclature

$\overline{\overline{C}}$	inertial resistance coefficient tensor (m^{-1})	P_2	regenerator exit pressure (Pa)
$\overline{\overline{c_f}}$	Forchheimer inertial coefficient tensor (–)	Re	Reynolds number (–)
$c_{f,i}$	directional Forchheimer inertial coefficient (–)		
E	fluid total specific energy (J/kg)	*Greek symbols*	
$\vec{F}_{bf}$	body force (N)	$\overline{\overline{\beta}}$	viscous resistance coefficient matrix (m^2)
f	friction factor	ε	porosity (–)
g	gravitational constant (=9.81 m/s^2)	μ	dynamic viscosity (kg/m s)
$\vec{g}$	gravitational acceleration (m/s^2)	ρ	density (kg/m^3)
h	specific enthalpy (J/kg)	$\overline{\overline{\tau}}$	stress tensor (N/m^2)
$\overline{\overline{I}}$	identity tensor		
$\overline{\overline{K}}$	Darcy permeability tensors (m^2)	*Subscripts*	
K_i	directional Darcy permeability (m^2)	f	fluid
k	thermal conductivity (W/m K)	r	radial
m	mass (kg)	s	solid
T	temperature (K)	t	turbulent
t	time (s)	x	axial
$\vec{u}$	volume-average intrinsic velocity (m/s)		
P_c	inlet pressure for annular test section (Pa)	*Superscript*	
P_1	regenerator inlet pressure (Pa)	T	transpose

boundary conditions by applying volume averaging [7–12]. Volume averaging and other similar methods lead to macroscopic and tractable governing equations which are consistent with micro-scale conservation principles, although they often mask much of the details related to pore-level processes. They also introduce constitutive relations that are needed for closure of macroscopic conservation equations. Without pore-level direct simulation, these macroscopic relations need to be specified empirically. Included among these relations are the Darcy permeability and Forchheimer's inertial coefficient tensors which need to be defined for the closure of the macroscopic momentum conservation equation.

Several investigator have measured and correlated the regenerator friction factors in steady-state or steady-periodic flow [13–16]. However, the present investigation is novel in its rigorous CFD-based determination of the hydrodynamic parameters.

In this paper, the hydrodynamic parameters associated with steady flow of helium in several common pulse tube and Stirling cryocooler fillers are measured and correlated. The hydrodynamic parameters associated with oscillatory flow of helium in the same regenerator fillers will be addressed in a separate forthcoming article [17].

2. Experiments

2.1. Regenerator fillers

Table 1 summarizes the geometric and structural characteristics of the regenerator fillers that were investigated. The common approach for constructing a regenerator is to fill its housing with a stack of microscreen sheets, micromachined perforated plates, or metal foam pellets, etc., and adjust its porosity by proper packing. It is therefore reasonable to assume that these porous regenerators are axisymmetric.

Table 1
Characteristics of the tested porous structures

Porous matrix type	Length/diameter (mm)	Wire diameter/pore diameter	Porosity (%)	Material
Tested regenerators for axial flow tests				
325 Mesh screen	38.1/7.94	35.6 μm	69.2	Stainless steel
400 Mesh screen	38.1/7.94	25.4 μm	69.2	Stainless steel
Sintered 400 mesh	38.1/7.94	Sintered	62	Stainless steel
Foam metal	38.1/7.94	Sintered	55.47	Stainless steel
Micro-machined disks[a]	31.4/15	36–40 μm	26.8	Nickel
	OD/ID/length (mm)	Wire diameter		
Tested regenerator for radial flow test				
325 Mesh screen/annular geometry	20/4/11.43	35.6 μm	69.6	Stainless steel

[a] Provided by International Mezzo Technologies Inc. Baton Rouge, Louisiana.

2.2. Steady-state radial pressure drop apparatus and procedures

A schematic of the apparatus is shown in Fig. 1. It includes a helium tank, a mass flow meter, two pressure transducers, and a specially designed annular test section that is packed with the regenerator fillers. The helium had a nominal purity of 99.9999%. By manually adjusting the valves V1 and V2, the flow rate and the pressure at the inlet to the test section, P_1, can both be adjusted. The exit from the annular test section was open to the atmosphere.

Details of the test section and its vicinity are depicted in Fig. 2. The test section consists of a straight 3.175 mm inner diameter circular tube that leads to an annular test section. When 325 stainless steel mesh screen are of interest, for example, a stack of these screens is used which forms an 11.43 mm long porous structure with an inner diameter of 4 mm and an outer diameter of 20 mm. Test section dimensions for all tested regenerator fillers are summarized in Table 1. The annular structure was constructed by threading three stainless steel rods perpendicular to an aluminum disk 30 mm long and 90 mm in diameter. A 3.175 mm diameter hole was drilled through the aluminum disk which served as the inlet channel to the annular porous structure. The three rods were equally spaced such that a 20 mm diameter cylinder could be tightly housed between them. They formed three rigid supports for stacking 20 mm diameter annular screens with a 4 mm inner diameter between them. The micro-screens, prepared by laser cut procedure, were provided by Cleveland Wire, Inc. and were stacked, pressed, and fitted between two rubber seals. The free ends of the stack (right side in Fig. 2) was sealed off by pressing a circular, 5 mm thick aluminum disk against the filler and then tightening the three hexagonal nuts at the ends of each threaded rod. The constructed test section thus formed a leak free system where gas could only escape in the radial direction through the outer, lateral surface of the annular porous structure. By tightening or loosening the nuts on the threaded rods, the volume of the porous filler could be slightly adjusted to obtain the desired porosity.

The porosity of the test section was measured by measuring the test section's volume, and measuring its weight before and after loading it with fillers. The weight difference, when divided by the filler material density, would then provide the total filler volume in the test section.

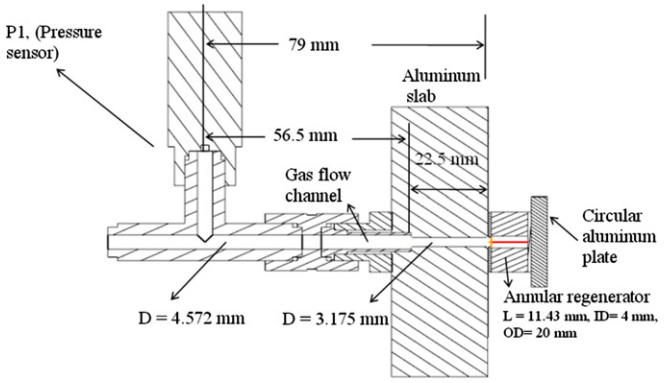

Fig. 2. Detailed view of the radial test section and its vicinity.

The mass flow meter (model 826 Toptrak, from Sierra Instruments) had a response time of 800 ms, a range of 0–1.5 g/s, and an accuracy of ±1.5% of its full range. A repeatability of ±0.5% of full range was obtained in the tests. Pressure readings were taken using two pressure transducers (series 210-10, Paine Electronics) with an adjusted range of 0–2757 kPa, and accuracy of ±0.25% of full range, and a maximum repeatability error of ±0.5% of full range.

A series of tests was performed for each regenerator filler and porosity. Each series was conducted by varying the steady-state mass flow rate and increasing the flow rate with valve V1, starting from a very low flow rate, increasing the flow by increments, and measuring the pressure at P_1. The errors associated with the measured pressure drop and mass flow rate were estimated to be ±6.8925 kPa and ±0.0225 g/s, respectively, based on the accuracy of the measurement instruments and the data recording system.

2.3. Steady-state axial pressure drop apparatus and procedures

The schematic of the apparatus for the axial steady-flow tests is shown in Fig. 3. The apparatus includes a tank of compressed helium, a pressure regulator, the test section, and valves 1 and 2 which are used in combination for the adjustment of the helium flow rate and average pressure

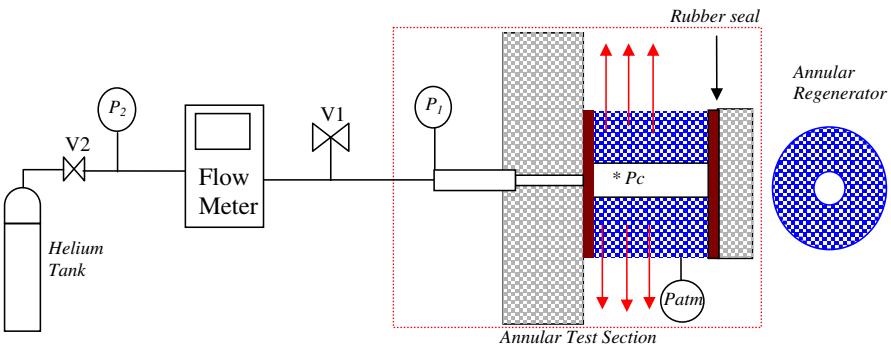

Fig. 1. Schematic of radial pressure drop test apparatus for steady flow.

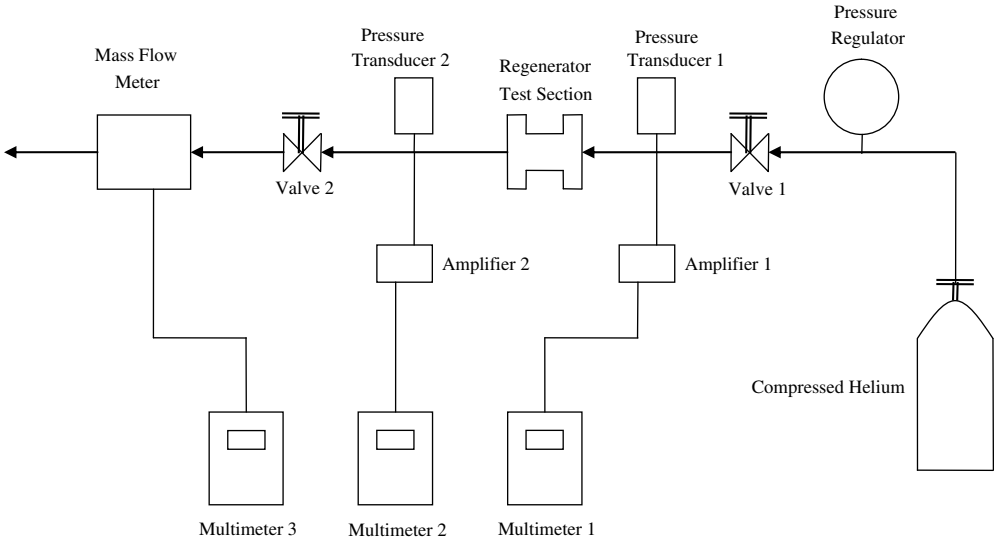

Fig. 3. Axial pressure drop experimental apparatus diagram.

within the porous filler. The pressures at the two ends of the test section are measured using pressure transducers similar to those utilized for radial pressure drop apparatus. The analog mass flow meter (Model 826 Toptrak, Sierra Instruments) has an accuracy of 1.5% of its full range (1.5 g/s). Fig. 4 displays the details of the test section and its vicinity. The test section is made of aluminum, and consists of a housing for porous test samples 3.81 cm in length with a diameter of 0.794 cm. This test section was used for all of the porous fillers except for the micromachined disks. For the micromachined disks a similar test section was used except that the housing for the regenerator filler was 3.14 cm in length with a 1.5 cm diameter.

The regenerator housing was carefully packed with the desired regenerator material at the desired porosity and special care was taken to ensure that the apparatus was leak tight prior to testing. The pressure regulator was set to 2068 kPa for most of the tests with valve 1 completely open and valve 2 completely closed. As valve 2 was slowly opened, fluid flow was initiated and the values of inlet pressure, outlet pressure, and mass flow were measured. Note that unlike the radial flow test section, which is open to the atmosphere at its exit, the presence of valve 2 allows for the adjustment of the pressure at the outlet of the axial flow test section.

The total error associated with the measured pressure drop across the porous fillers was estimated to be ±9.8 kPa. The estimated error in the mass flow rate measurement was 0.0225 g/s. These estimates were based on the accuracy of the measurement instruments and the data recording system. More details can be found in [20].

3. Experimental results

Figs. 5 and 6 display the pressure drops measured in the steady, radial flow test apparatus (i.e., $P_1 - P_{atm}$ in Fig. 1) for 325 mesh screens. Each test series was conducted by varying the steady-state mass flow rate with valve V1 starting from a very low value and increasing the flow rate by small increments while measuring the pressure P_1 at each interval. Three test series were performed for the 325 mesh filler at 69.6% porosity to examine reproducibility and, as indicated in Fig. 5, excellent reproducibility was demonstrated. In Fig. 6, the total measured pressure drop ($P_1 - P_{atm}$) for 325 mesh as well as the pressure drop across the porous annular structure (defined as $P_c - P_{atm}$, with P_c representing the pressure of point C in Fig. 1) are shown. The latter pressure drop is the result of the forthcoming CFD simulations.

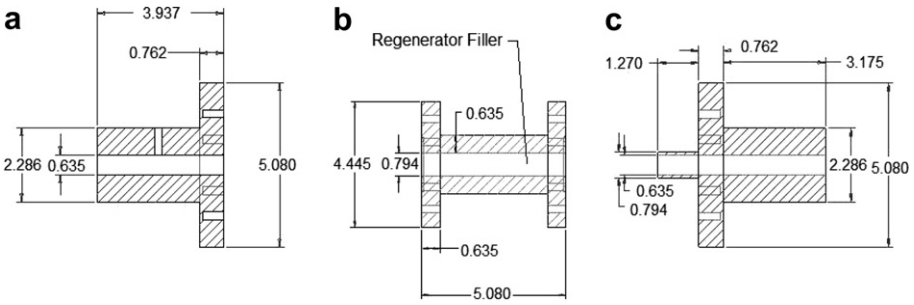

Fig. 4. Detailed test section of the axial test apparatus (dimensions in cm).

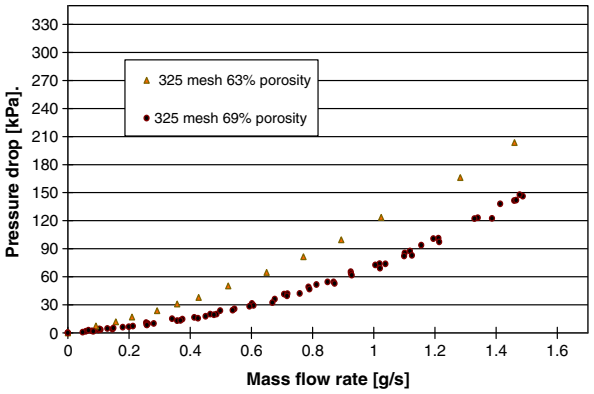

Fig. 5. Experimental radial pressure drops for 325 mesh stacked screens.

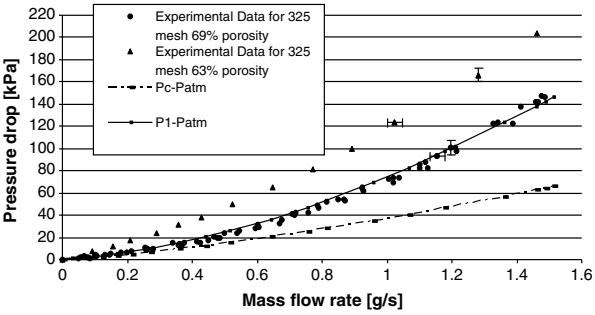

Fig. 6. Experimental radial/lateral pressure drops and simulated results.

Figs. 7–10 depict the pressure drop data associated with the steady axial flow test apparatus (see Figs. 3 and 4). The data in Figs. 7, 8 and 10 were all obtained with a supply pressure of 2068 kPa. In order to examine the effect of pressure on the hydrodynamic parameters, four separate series of tests were performed with the sintered 400 mesh screens and these data are displayed in Fig. 9. The measurements associated with three repetitive test series with a supply pressure of 2757 kPa (Run 3) are also shown in the figure. The repeatability is evidently very good. An important note

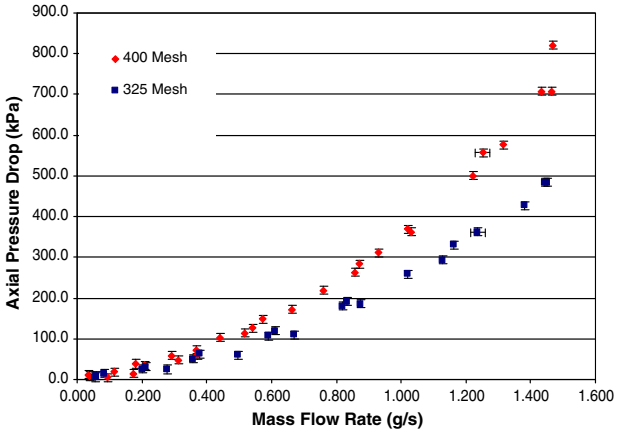

Fig. 7. Steady-flow axial pressure drop for 325 and 400 mesh −69.69% porosity.

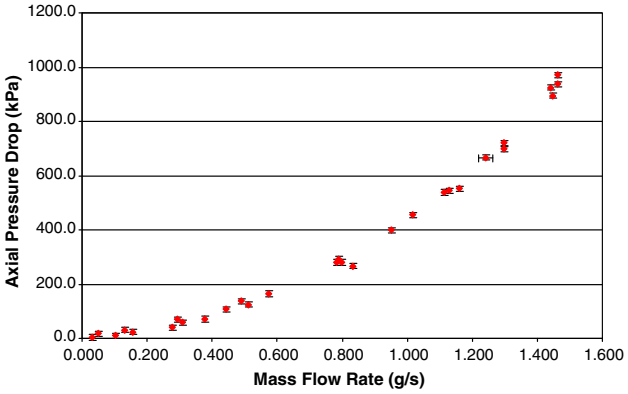

Fig. 8. Steady-flow axial pressure drop for stainless steel metal foam −55.47% porosity.

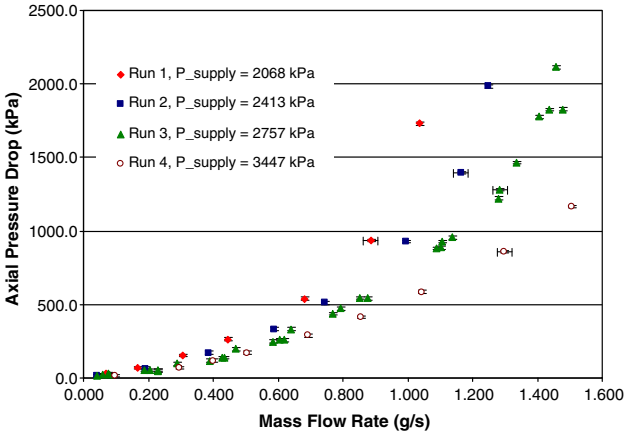

Fig. 9. Steady-flow axial pressure drop for sintered 400 mesh −61.65% porosity.

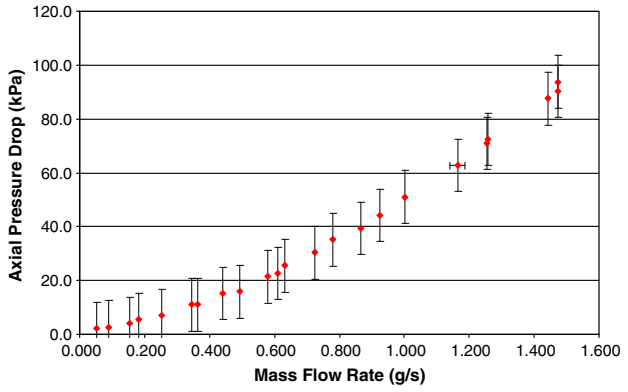

Fig. 10. Steady-flow axial pressure drop for micromachined disks −26.8% porosity.

in Fig. 9 is that the pressure drop is a function of flow rate and the mean pressure in the porous test section.

Fig. 10 shows the pressure drop test results for the stacked perforated nickel disks at 26.8% porosity. These structures provide a much lower pressure drop than the other tested samples. The measured pressure drop for the micromachined disks was typically over an order of magnitude smaller than that of the metal foam and the

sintered mesh samples. As a result, while the results exhibited good repeatability, be noted that the error associated with the pressure transducers for the micromachined disk samples was very high relative to the magnitude of the pressure drop.

3.1. Analysis and interpretation of data

A CFD-assisted method was used for the analysis and interpretation of the experimental data in order to avoid the use of arbitrary assumptions. The commercial CFD code Fluent [18] and the mesh generation package Gambit [19] were used for modeling purposes. For each test, the entire test section and its vicinity were finely discretized and modeled. Iterative numerical simulations were then performed by adjusting the hydrodynamic parameters in the CFD model which eventually led to close matching between the experimental data and the simulated results.

Fig. 11 displays the discretized model of the steady-state radial flow test section where approximately 5500 mesh nodes have been used. The effect of the number of nodes on the simulated results was examined by increasing the number of nodes for selected runs by a factor of two. This increase in mesh resolution led to negligibly small changes in the simulated results. These simulated models contain two different parts: an open part that supports a pure single-phase gas flow, and a porous solid structure. For the open parts, the following general continuum-based governing equations apply and are solved by Fluent:

$$\frac{\partial \rho}{\partial t} + \nabla \cdot (\rho \vec{u}) = 0, \tag{1}$$

$$\frac{\partial}{\partial t}(\rho \vec{u}) + \nabla \cdot (\rho \vec{u}\vec{u}) + \nabla P - \nabla \cdot \bar{\bar{\tau}} - \rho \vec{g} = 0, \tag{2}$$

$$\left\{ \langle k \nabla T \rangle + (\bar{\bar{\tau}} \cdot \vec{u}) \right\} - \frac{\partial}{\partial t}(\rho E) - \nabla \cdot (\vec{u} \langle \rho E + P \rangle) = 0, \tag{3}$$

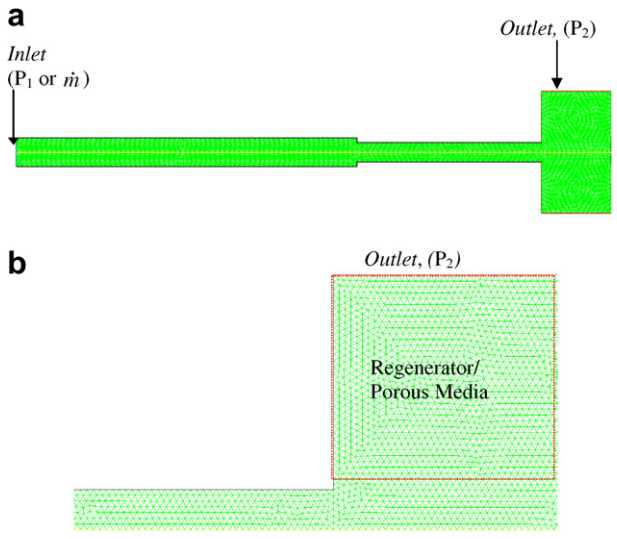

Fig. 11. CFD model of the steady radial flow test section: (a) entire simulated system; (b) porous structure.

where

$$E = h - \frac{P}{\rho} + \frac{u^2}{2}, \tag{4}$$

$$\bar{\bar{\tau}} = \mu \left[(\nabla \vec{u} + \nabla \vec{u}^{\mathrm{T}}) - \frac{2}{3} \nabla \cdot \vec{u} \bar{\bar{I}} \right]. \tag{5}$$

For the porous parts of the test section, local thermal equilibrium between the fluid and the porous structure was assumed everywhere and the following governing equations were solved [18]:

$$\frac{\partial (\varepsilon \rho)}{\partial t} + \nabla \cdot (\varepsilon \rho \vec{u}) = 0, \tag{6}$$

$$\frac{\partial}{\partial t}(\varepsilon \rho \vec{u}) + \nabla \cdot (\varepsilon \rho \vec{u}\vec{u}) + \varepsilon \nabla P + \nabla \cdot (\varepsilon \bar{\bar{\tau}} t) - \varepsilon \vec{F}_{\mathrm{bf}} + \frac{\mu}{\bar{\bar{\beta}}} \cdot \vec{u} + \frac{\bar{\bar{C}} \rho}{2} \cdot |\vec{u}| \vec{u} = 0, \tag{7}$$

$$\nabla \cdot \langle [\varepsilon k_{\mathrm{f}} + (1-\varepsilon) k_s] \nabla T + (\bar{\bar{\tau}} \cdot \varepsilon \vec{u}) \rangle = \frac{\partial}{\partial t}(\varepsilon \rho_{\mathrm{f}} E_{\mathrm{f}} + (1-\varepsilon) \rho_s E_s) + \nabla \cdot (\varepsilon \vec{u} \langle \rho_{\mathrm{f}} E_{\mathrm{f}} + P \rangle), \tag{8}$$

where ε is the porosity, $\vec{F}_{\mathrm{bf}}$ is the body force and is equal to $\rho \vec{g}$ when gravity is the only source of body force, and $\bar{\bar{\beta}}$ (m^2) and $\bar{\bar{C}}$ (m^{-1}) are the viscous and inertial resistance coefficient tensors, respectively. These equations are based on volume averaging of conservation equations for porous media, and the application of commonly used closure relations [11,12]. The velocity $\vec{u}$ represents the volume-averaged intrinsic (physical) fluid velocity. The tensors $\bar{\bar{\beta}}$ and $\bar{\bar{C}}$ will be diagonal when the coordinates coincide with the principle directions of the porous medium and become constant scalars for an isotropic medium. The assumption of axisymmetry implies that the axial and any radial directions are principle directions. For an isotropic porous medium the last two terms of Eq. (7) reduce to the left side of the following equation:

$$\frac{\mu}{\beta} \vec{u} + \frac{C \rho}{2} |\vec{u}| \vec{u} = \frac{\varepsilon^2 \mu}{K} \vec{u} + \frac{c_{\mathrm{f}} \varepsilon^3 \rho}{\sqrt{K}} |\vec{u}| \vec{u}, \tag{9}$$

where β and C are now constant scalars, and K and c_{f} are the permeability and Forchheimer's inertial coefficients, respectively. Eq. (9) thus depicts the relationship among β and C on one side and K and c_{f} on the other. Therefore,

$$K = \varepsilon^2 \beta, \tag{10}$$

$$c_{\mathrm{f}} = \frac{C \sqrt{K}}{2 \varepsilon^3}. \tag{11}$$

We can extend the above to an anisotropic medium. For coordinate i when it is a principle direction, we will write

$$\frac{\mu}{\beta_i} u_i + \frac{C_i \rho}{2} |\vec{u}| u_i = \frac{\varepsilon^2 \mu}{K_i} u_i + \frac{c_{\mathrm{f},i} \varepsilon^3 \rho}{\sqrt{K_i}} |\vec{u}| u_i, \tag{12}$$

where

$$K_i = \varepsilon^2 \beta_i, \tag{13}$$

$$c_{f,i} = \frac{C_i \sqrt{K_i}}{2\varepsilon^3}. \tag{14}$$

An alternative to the definition of viscous resistance and inertial resistance coefficients is the friction factor defined according to

$$0.5 \frac{f_i}{\sqrt{\beta_i}} \rho |\vec{u}| u_i = \frac{\mu}{\beta_i} u_i + \frac{C_i \rho}{2} |\vec{u}| u_i. \tag{15}$$

By non-dimensionalizing Eq. (15), the friction factor can be recast as

$$f_i = \frac{2}{Re_{\beta_i}} + C_i \sqrt{\beta_i}, \tag{16}$$

where Re_{β_i} is the local Reynolds number defined as

$$Re_{\beta_i} = \frac{\rho |\vec{u}| \sqrt{\beta_i}}{\mu}. \tag{17}$$

Eqs. (16) and (17) can also be written as

$$f_i = \frac{2\varepsilon}{Re_{K_i}} + 2C_i \varepsilon^2, \tag{18}$$

$$Re_{K_i} = \frac{\rho |\vec{u}| \sqrt{K_i}}{\mu}. \tag{19}$$

All the simulations were performed using a residual convergence criterion of 1.0e−8 for the mass, x-velocity, r-velocity, and energy. Second order upwind discretization scheme (SOUDS) was initially applied. However, much better residual convergences were noticed using the first order upwind discretization scheme (FOUDS). Thus, all CFD models were re-simulated using the FOUDS. The boundary conditions included known pressure P_1 or mass flow at the inlet (see Fig. 1), and atmospheric exit conditions.

The axial flow test section and its vicinity were similarly discretized and meshed using approximately 2200 nodes. The effect of mesh size was tested by repeating selected simulations with twice as many nodes and was found to be negligibly small. Simulations were iteratively repeated for each specific test by adjusting the permeability and Forchheimer's inertial coefficient or, equivalently, the viscous and inertial resistance coefficients, until the simulated test section exit conditions matched the measurements. More details can be found in [20,21].

The mesh resolution (cell width) in the simulations was about 350 μm. In comparison, the mesh size was about 70 μm × 70 μm for the 350 mesh screens, and 55 μm × 55 μm for the 400 mesh screens, respectively.

It should be mentioned that laminar flow has been assumed in the above formulation. For steady flow, laminar-turbulent transition occurs at a critical Reynolds number of $Re_K \approx 350$ [22–24]. The experimental data in this study represented $Re_K < 10$, however.

4. Results and discussion

4.1. Radial flow tests

CFD Simulations were performed for the tests with $\varepsilon = 0.696$. Harvey [3] previously measured the axial flow parameters for an identical porous matrix with $\varepsilon = 0.696$, and obtained $\beta_x = 5.0711\text{e}{-11}\ \text{m}^2$ and $C_x = 61{,}330\ \text{m}^{-1}$. These values were used in two-dimensional simulations which were iteratively repeated while adjusting β_r and C_r. Very good agreement between data and simulated results was obtained with $\beta_r = 1.4705\text{e}{-10}\ \text{m}^2$ and $C_r = 98{,}600\ \text{m}^{-1}$. Fig. 6 compares the measured total pressure drops with the results of the simulations using the latter parameter values. As noted, β_r is approximately three times larger than β_x, confirming the importance of anisotropy in the tested filler. The steady radial hydrodynamic parameters are summarized in Table 2.

Fig. 12 depicts the velocity vectors in the radial flow test section for two typical simulations. As noted in Fig. 12A, at very low mass flow rates the velocity vectors in the annular porous medium were approximately purely radial. At higher mass flow rates, represented by Fig. 12B, however, significant two-dimensional effects occurred near the blocked end of the test section. The occurrence of these complex, multidimensional flow effects only confirmed that correct extraction of the hydrodynamic parameters requires a detailed CFD-based analysis.

4.2. Axial flow tests

Table 3 summarizes the axial steady flow, axial hydrodynamic parameters for the tested regenerator fillers. The uniqueness of the values reported in Table 3 and the sensitivity of the simulated pressure drop with respect to the hydrodynamic parameters can be seen in Fig. 13. (Note that parameter D_x follows the general definition $D_i = 1/\beta_i$.) For the sintered 400 mesh sample, multiple simulations were conducted for many different combinations of D_x and C_x. For each of these cases, the average percent difference between the simulated pressure drop and the actual pressure drop in the test section were calculated. The square in Fig. 13 represents the steady-flow viscous and inertial resistances for sintered 400 mesh as reported in Table 3. Each one of the circular points represents subsequent simulations that were performed using different values of the hydrodynamic parameters. Each contour represents the average percent difference between the simulated pressure drop and the actual pressure drop. It can be seen that there is a local minimum which represents the values of D_x and C_x that would result in the smallest error. Therefore, it can be concluded

Table 2
Results of steady radial hydrodynamic parameters for SS 325 mesh

Annular regenerator	β_r (m^2)	C_r (1/m)	K_r (m^2)	$c_{f,r}$ (–)
325 mesh screens	1.4705e−10	98,600	7.0011e−11	1.256

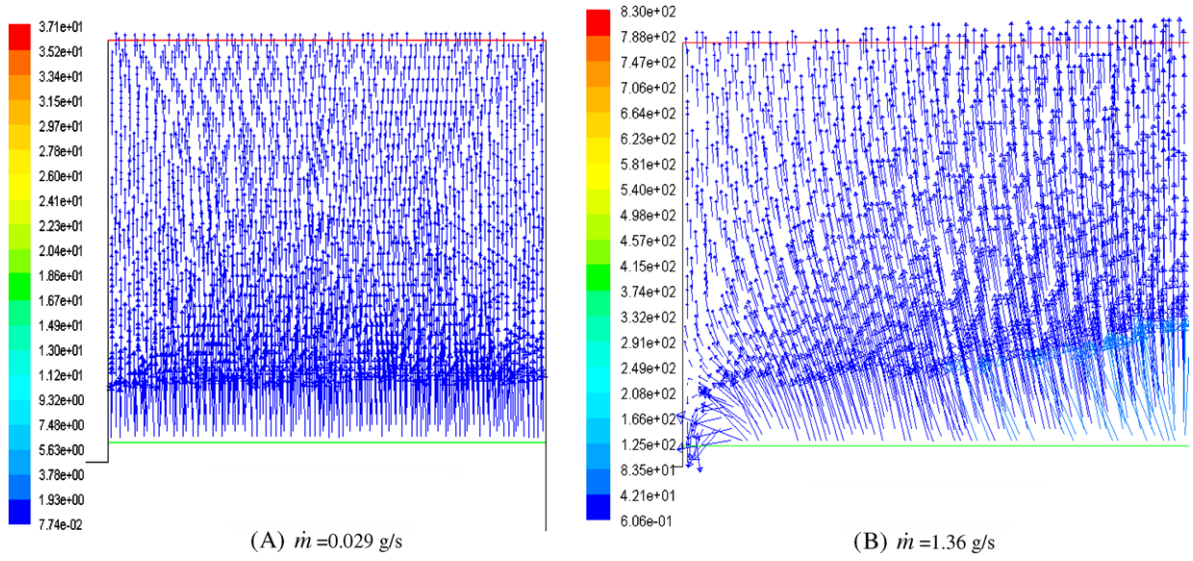

Fig. 12. Steady velocity vectors (in m/s) in 325 mesh regenerator with $\varepsilon = 0.696$. The vertical coordinate is in the radial direction.

Table 3
Steady-flow axial hydrodynamic parameters

RegeneratorMaterial	Porosity (%)	β_x (m^2)	C_x (1/m)	K_x (m^2)	$c_{f,x}$ (–)
400 Mesh	69.69	3.61e−11	73000	1.753e−11	0.452
325 Mesh	69.69	4.25e−11	47000	2.067e−11	0.316
400 Sintered (2068 kPa)	61.65	1.69e−11	259768	6.444e−12	1.407
400 Sintered (2413 kPa)	61.65	1.72e−11	250104	6.538e−12	1.365
400 Sintered (2757 kPa)	61.65	1.76e−11	235594	6.689e−12	1.300
400 Sintered (3447 kPa)	61.65	1.82e−11	215834	6.916e−12	1.211
Metal foam	55.47	3.72e−11	99000	1.161e−11	0.988
Machined disk	26.80	4.35e−11	115000	3.123e−12	5.279

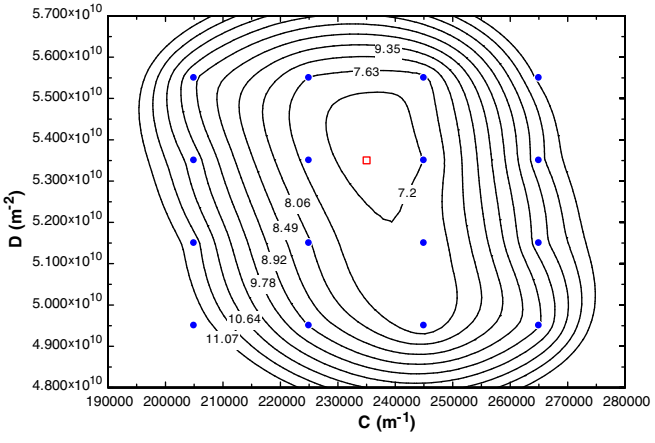

Fig. 13. Average percent difference contours (%) vs. D_x and C_x for sintered 400 mesh with a 2757 kPa (400 psi) supply pressure.

that, for the range of D_x and C_x shown in Fig. 13, there will exist unique values of the hydrodynamic parameters that will provide the most accurate prediction.

The sensitivity of the CFD model to changing D_x and C_x can also be obtained from Fig. 13. For the sintered 400 mesh sample, the viscous resistance may be varied by about ±3% and the inertial resistance varied by about ±5% without significantly changing the accuracy of the simulation.

These hydrodynamic parameters can also be expressed in non-dimensional terms. Fig. 14 is the steady-flow friction factor, f_x, as defined by Eq. (18) for all of the samples at the stated porosity. The average gas density in the porous section was used for calculating Re_K and f.

4.3. Effects of pressure and anisotropy

All the axial flow experimental data discussed thus far were obtained with a supply line pressure of 2068 kPa. Using the sintered 400 mesh sample, the effects of varying pressure on the hydrodynamic parameters was also examined. This was done by performing three more complete test series at 2413, 2757, and 3447 kPa supply pressures. The aforementioned CFD-assisted procedure was then

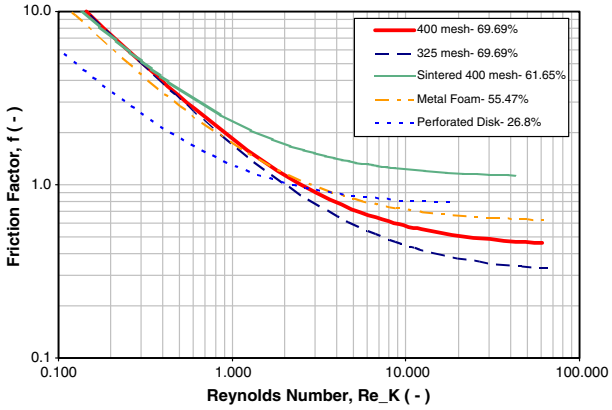

Fig. 14. Steady-flow axial friction factors for $P_{supply} =$ 2068 kPa.

applied to each test series leading to the calculation of separate values of β_x and C_x for each series. Noting that the values of the hydrodynamic parameters were affected by pressure, the following correlations were developed:

$$\beta_x = \beta_0 \left[\frac{P_{avg}}{P_{cr}}\right]^{n_1}, \tag{20}$$

$$C_x = C_0 \left[\frac{P_{avg}}{P_{cr}}\right]^{n_2}, \tag{21}$$

where P_{avg} is the average pressure in the porous material, P_{cr} is the critical pressure of helium, and $\beta_0 = 1.504\text{e}{-11}\ \text{m}^2$; $n_1 = -0.08$; $C_0 = 3.65\text{e}5\ \text{m}^{-1}$; $n_2 = -0.21$.

These constants were iteratively determined by seeking the minimum average error between the adjusted hydrodynamic parameters as calculated by Eqs. (20) and (21) and the actual parameters determined the CFD analysis of the experimental data. These constants are unique to the sintered 400 mesh. Fig. 15 compares the simulated results using the pressure dependent hydrodynamic parameters with the experimental data.

A comparison between the axial and radial hydrodynamic parameters for the 325 mesh screen regenerator in Tables 2 and 3 confirms the significance of anisotropy in common regenerator fillers. The radial and axial friction factors for this regenerator filler are plotted together in Fig. 16, and display clearly the significant difference between these two directional friction factors.

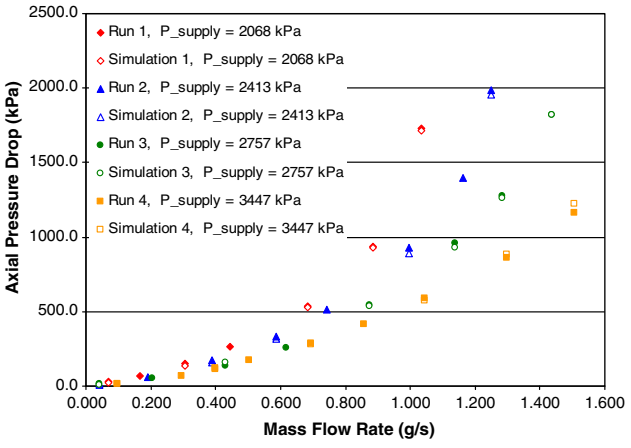

Fig. 15. Simulation vs. experimental pressure drop using pressure dependent hydrodynamic parameters: sintered 400 mesh 61.65% porosity.

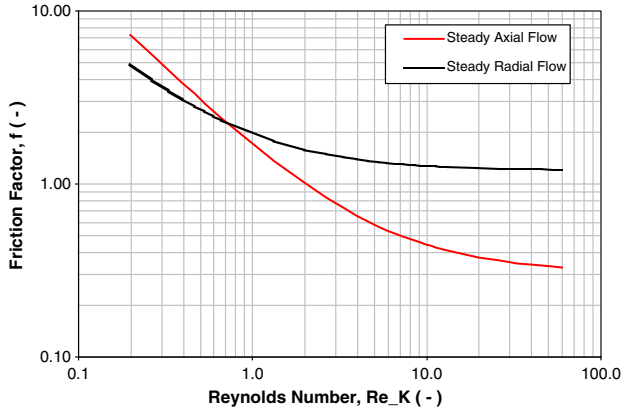

Fig. 16. Anisotropic steady-flow friction factor for 325 mesh screens – 69.69% porosity.

5. Concluding remarks

In this investigation, experiments were performed for the measurement and correlation of axial and radial viscous and inertial resistance parameters associated with steady flow of helium in some common cryocooler regenerator structures. The data analysis was performed using a CFD-assisted method. The structures studied for axial flow resistance parameters were stacked 325 mesh screens, stacked 400 mesh screens, sintered 400 mesh screens, metal foam, and aligned micromachined nickel disks with 36–40 μm diameter holes. Radial flow resistance parameters were also measured for stacked 325 mesh screens. A CFD-assisted method was applied for the analysis and interpretation of the experimental data. The test sections and their vicinity were modeled with the regenerator filler represented as a porous zone and the viscous and inertial coefficients (or, equivalently, the permeability and Forchheimer's inertial coefficient) were iteratively adjusted to bring about agreement between the measured pressure drop and the simulated results. Accordingly, the permeability and inertial coefficients were reported for the aforementioned porous structures. The results confirm the importance of anisotropy and average pressure in the porous structures of the tested regenerator fillers.

The experimental data discussed in this paper dealt only with steady flow, but cryocoolers operate in periodic flow conditions. Experimental data and modeling schemes dealing with oscillatory helium flow in the aforem entioned regenerator fillers will be discussed in [17].

References

[1] Gifford WE, Longsworth RC. Pulse-tube refrigeration. ASME Paper No. 63-WA-290 presented at the Winter Annual Meeting in Philadelphia, PA, November; 1963. p. 17–22.
[2] Gifford WE, Longsworth RC. Surface heat pumping. Advances in cryogenic engineering, vol. 11. New York: Plenum Press; 1968. p. 171–9.
[3] Harvey J. Oscillatory compressible flow and heat transfer in porous media-application to cryocooler regenerators. PhD thesis, Atanta, Ga: Georgia Institute of Technology; 2003.
[4] Radebaugh R. Development of the pulse tube refrigerator as an efficient and reliable cryocooler. National Institute of Standards and Technology. In: Proc. institute of refrigeration, London; 1999–2000.
[5] Flakes B, Razani A. Modeling pulse tube cryocoolers with CFD. In: Proc. international cryogenics engineering conference; September 2003. p. 1493–9.
[6] Cha JS, Ghiaasiaan SM, Desai PV, Harvey JP, Kirkconnel CS. Multi-dimensional flow effects in pulse tube refrigerators. Cryogenics 2006;46:658–65.
[7] Cha JS. Hydrodynamic parameters of microporous media for steady and oscillatory flow: application to cryocooler regenerators. PhD thesis, Georgia Institute of Technology, Atlanta, GA; 2007.

[8] Ochoa-tapia J, Whitaker S. Heat transfer at the boundary between a porous medium and a homogeneous fluid. Int J Heat Mass Transfer 1997;40(11):2691–707.
[9] Ochoa-tapia J, Whitaker S. Momentum transfer at the boundary between a porous medium and a homogeneous fluid – I. Theoretical development. Int J Heat Mass Transfer 1995;38(14):2635–46.
[10] Ochoa-tapia J, Whitaker S. Momentum transfer at the boundary between a porous medium and a homogeneous fluid – II. Comparison with experiment. Int J Heat Mass Transfer 1995;38(14):2647–55.
[11] Whitaker S. The method of volume averaging. Dordrecht: Kluwer Academic; 1999.
[12] Whitaker. The Forchheimer equation: a theoretical development. Transport in porous media, vol. 25. Netherlands: Kluwer Academic Publishers; 1996. p. 27–61.
[13] Zhao TS, Cheng P. Cryogenics 1996;36:1619–26.
[14] Jeong S, Nam K, Jung J. Regenerator characterization under oscillating flow and pulsating pressure. Cryocoolers 2002;12: 531–7.
[15] Kaviany M. Principles of heat transfer in porous media. 2nd ed. New York: Springer-Verlag; 1995.
[16] Nam K, Jeong S. Experimental study on the regenerator under actual operating conditions. Adv Cryog Eng 2002;47:977–84.
[17] Cha JS, Ghiaasiaan SM, Kirkconnell CS. Oscillatory flow in microporous media applied in pulse – tube and Stirling – cycle cryocooler regenerators. Int J Exper Therm Fluid Sci, in press.
[18] Fluent INC. Fluent 6 User Manual; 2003. p. 8-1.
[19] Fluent INC. Gambit User Manual.
[20] Clearman WM. Measurement and correlation of directional permeability and forchheimer's inertial coefficient of micro porous structures used in pulse tube cryocoolers. Masters thesis, Atlanta (GA): Georgia Institute of Technology; 2007.
[21] Cha JS. CFD Simulation of multi-dimensional effects in inertance tube pulse tube cryocoolers. Master's thesis, Atlanta (GA): Georgia Institute of Technology; 2004.
[22] Dybbs A, Edwards RV. New look at porous media fluid mechanics – Darcy to turbulent. NATO ASI Ser, Ser E: Appl Sci 1984;82:199–256.
[23] Liu S, Afacan A, Masliyah J. Steady incompressible laminar flow in porous media. Chem Eng Sci 1994;49:3565–86.
[24] Pedras MHJ, De Lemos MJS. Macroscopic turbulence modeling for incompressible flow through undeformable porous media. Int J Heat Mass Transfer 2001;44:1081–93.